Propulsion mechanism of artificial flagellated micro-swimmers actuated by acoustic waves—theory and experimental verification

Bioinspiration & Biomimetics

OPEN ACCESS

RECEIVED
16 May 2024

REVISED
2 July 2024

ACCEPTED FOR PUBLICATION
11 July 2024

PUBLISHED
23 July 2024

PAPER

Propulsion mechanism of artificial flagellated micro-swimmers actuated by acoustic waves—theory and experimental verification

Jinan Liu, Yiqiang Fu, Yifei Wu and Haihui Ruan*

Research Center for Fluid-Structure Interactions, Department of Mechanical Engineering, The Hong Kong Polytechnic University, Hung Hom, Kowloon, Hong Kong Special Administrative Region of China, People's Republic of China

* Author to whom any correspondence should be addressed.

E-mail: hhruan@polyu.edu.hk

Keywords: artificial micro-swimmer, acoustic actuation, experimental verification, materials characterization

Supplementary material for this article is available online

Abstract

This work examines the acoustically actuated motions of artificial flagellated micro-swimmers (AFMSs) and compares the motility of these micro-swimmers with the predictions based on the corrected resistive force theory (RFT) and the bar-joint model proposed in our previous work. The key ingredient in the theory is the introduction of a correction factor K in drag coefficients to correct the conventional RFT so that the dynamics of an acoustically actuated AFMS with rectangular cross-sections can be accurately modeled. Experimentally, such AFMSs can be easily manufactured based on digital light processing of ultra-violet (UV)-curable resins. We first determined the viscoelastic properties of a UV-cured resin through dynamic mechanical analysis. In particular, the high-frequency storage moduli and loss factors were obtained based on the assumption of time-temperature superposition (TTS), which were then applied in theoretical calculations. Though the extrapolation based on the TTS implied the uncertainty of high-frequency material response and there is limited accuracy in determining head oscillation amplitude, the differences between the measured terminal velocities of the AFMSs and the predicted ones are less than 50%, which, to us, is well acceptable. These results indicate that the motions of acoustic AFMS can be predicted, and thus, designed, which pave the way for their long-awaited applications in targeted therapy.

1. Introduction

The rapid development of micro-robotics in the past two decades has benefited from the advance of micro-nano technology and smart materials [1]. These small-scale devices have drawn widespread attention because of the great application prospect in, for example, the medical cargo delivery [2–6] and water remediation [7–9]. Nevertheless, most of studies are concentrated on laboratory demonstrations [10, 11] where the micro-robots, i.e. the artificial micro-swimmers, are shown in various designs, such as bubbles [12, 13], nanorods [14, 15], helical filaments [16, 17], and flagella [18, 19]. The structure we focus on in this article is an artificial flagellated micro-swimmer (AFMS), which incorporates a relatively rigid head and a flexible tail, where the tail is commonly named a flagellum in microbiology [20]. We focus on the flagellated, a.k.a. sperm-like, structure because its rigid head has the potential for cargo delivery, which can lay the foundation of targeted therapy for cancer treatment [21]. Besides, this design is simple to fabricate through layer-by-layer photocuring (i.e. 3D printing) [19, 22], which will be presented in this work. Note that artificial micro-swimmers, like microorganisms, swim in a low-Reynolds-number (LRN) regime, requiring swimming strategies different from the macro-scale counterparts [23]. Researchers have proposed some methods to remotely drive and control micro-swimmers [24–26], such as optical [27], thermal [28], magnetic [29], and acoustic actuation [30]. Concerning medical applications, the driving strategy herein is limited to the acoustic actuation due to the requirements of bio-compatibility and medium-independence [31].

The directional motions of AFMSs under the acoustic actuation were observed in some experiments [18, 19]. Authors therein considered that the propulsion arose from the strong acoustic streaming around sharp edges of AFMSs, which is a well-established mechanism for propelling swimmers excited by acoustic waves [32–34]. However, it is generally complex to obtain acoustic streaming surrounding a micro-swimmer (mainly via numerical simulation based on the perturbation technique [34]), which gives rise to the difficulty of theoretical analyses, and sometimes, leads to significant discrepancies (e.g. the resonance frequency of the simulated value differs from the experimental observation in [18]). Fortunately, if a body is slender (i.e. the ratio of the characteristic width to length is less than 0.1 [35]), an asymptotic expression of fluid forces around solid boundaries can be obtained, known as the resistive force theory (RFT) [36–42]. Gray and Hancock [43] and Lighthill [44] developed the RFT to describe LRN swimming problems. Recently, in the analyses of artificial micro-swimmers, the RFT is the most adopted [14, 45, 46]. For example, studied in [14] and [46] were the micro/nano-rods propelled by ultrasound, wherein the complex effect of acoustic waves was simplified into forces estimated based on the drags calculated using the RFT owing to the LRN, which avoids the analysis of complexed acoustic streaming.

The above achievements inspired us to propose the mechanism of propulsion in our previous work [47], that is, acoustic waves lead to oscillations of the head of an AFMS, and the oscillating head beats the flagellum, which then propels the AFMS based on the RFT. Note that the effect of acoustic streaming is near the tip of a flagellum. Intuitively, the effect of the acoustic streaming can also be treated as forces causing flagellum wiggling but from the tail tip instead of the head. It is thus clear that the RFT can be widely employed to analyze the propulsion of an AFMS under the swimming mechanism we proposed. The problem with these studies is that the derivation of RFT is based on circular cross-sections, but the cross-sections of many artificial micro-swimmers are non-circular. For example, if a layer-by-layer photocuring is applied to fabricate AFMSs, the cross-section of the flagellum is more like a rectangle [19]. One may note that flagellated micro-swimmers with circular cross-sections can be manufactured [26], however, most of them are helical flagella [48] or nanorods synthesized using electrodeposition [18], which lack of a large head to load drugs for medical applications. In principle, the direct laser writing (DLW) technology [49] can break the optical diffraction limit and has a spatial resolution of nanometers, thus, it can be used to fabricate any shapes. Nevertheless, the photosensitive materials used for DLW technology are limited, and the cost may be high [26]. Instead, the digital light processing (DLP) [50] can improve the speed of sample fabrication, and has more selectivity for light sources, thus, it is very popular in the field of mass production of micro-swimmers with a large head (or a large dimension), especially via the in-situ fabrication [19, 51, 52], which are easy to manufacture and actuate. They have promising potential applications in many fields [53], and will also be employed in our experiments. However, due to the limited print resolution of our DLP printer, it is difficult to achieve non-rectangular cross-sections. Hence, we fabricated micro-swimmers with rectangular cross-sections. Hence, we proposed a corrected RFT (CRFT) model to correct the classical RFT for two-dimensional (2D) cases or flagellum with rectangular cross-sections. The theoretical process leads to a single correction factor K which can be determined by comparing the terminal swimming velocities obtained from the CRFT model with those from 2D fluid–structure interaction (FSI) simulations [54]. Nevertheless, the experimental verification of this theory is still unachieved.

Thus, the main purpose of this work is to verify the CRFT models by comparing terminal velocities of AFMSs observed in experiments to those predicted by theoretical calculation. In the subsequent sections, we describe the fabrication of AFMSs, the corresponding materials characterization, the experimental platform for acoustic actuation and observation, and the comparison between experiments and theoretical calculations (i.e. FSI simulations and CRFT models). Finally, we will discuss the insufficiency of this research.

2. Methodology

2.1. Fabrication

A commercial ultra-violet (UV) curable resin (Phrozen Water Washable Resin, Model Gray, Phrozen, Taiwan) [19, 22] was employed to fabricate AFMSs based on the technique of DLP due to its high dimensional precision and low fabrication cost. As shown in figure 1(a), a commercial 3D printer (Sonic Mini 8 K, Phrozen, Taiwan) was employed for photolithography with horizontal and vertical resolutions of 22 μm and 20 μm, respectively. Note that DLP printers can achieve higher precisions, such as those based on two-photon polymerization [55], and it may be needed in the future precision controls of AFMSs. In this work, to verify our theory, a low-cost DLP printer has suited the need.

A plate connected to a vertical guide and a lead screw is used as the base of printing, and at the bottom is a vessel containing a liquid photosensitive resin. During a layer-by-layer photocuring process at a UV wavelength of 405 nm, the plate is immersed in the resin solution. After printing, the plate can be detached from the guide and lead screw, and the product would generally be removed by a metal scraper. However, in this work, an AFMS to be

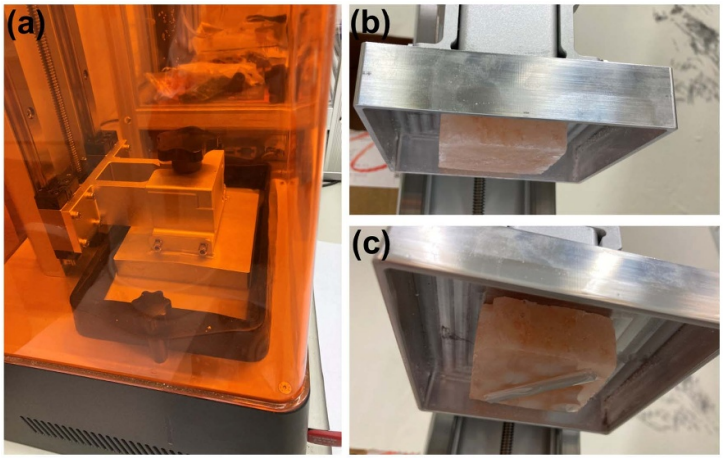

Figure 1. Fabrication of AFMSs and samples: (a) the 3D printer for photolithography with photosensitive resin inside its vat, and the building plate is immersed in the resin; (b) the modified building plate before photolithography, which is a rectangular cavity adhered with a salt brick; (c) after photolithography, the material sample is adhered to the salt brick.

printed is around 1–2 mm long and less than 0.5 mm thick, which is too small to be manually chipped. Therefore, we used a salt brick as the base of printing, as demonstrated in figure 1(b), and dissolved the salt brick in water to release printed products.

Figure 1(c) exhibits a rectangular sample (used for materials characterization) adhering to the salt brick after photocuring. Immersing the salt brick in water for some time, the sample can be shed. If the AFMSs are too small to be seen with the naked eye, it will be difficult to transfer them to an experimental platform to observe their motion. Hence, Kaynak *et al* [19] fabricated AFMSs *in situ*. Owing to the limitation of our laboratory equipment, transferring AFMSs from the printing stage to a testing channel is necessary (this will also be the case in future applications). Hence, we have to print AFMSs with a length over 1 mm to make them visible to human eyes and then transferable to an AFMS testing channel. Figures 2(a) and (b) exhibits the photos of the AFMSs tested in this work, taken by using an optical microscope. They are designated as L1 (i.e. figure 2(a) with 1 mm long) and L2 (i.e. figure 2(b) with 2 mm long), respectively. The thicknesses of L1 and L2 are homogeneous (0.3 mm for L1 and 0.5 mm for L2), which indicates that the cross-sections of these AFMSs are rectangular. Note that such a large dimension may lead to invalidity of the RFT if using water as the testing fluid, because the Reynolds number (Re) may be not sufficiently low. Hence, we used an aqueous solution for testing AFMSs, which is sodium polyacrylate (50% concentration, Macklin, China) with a viscosity of 0.1 Pa.s at room temperature. This ensures the Re in the range of 0.009–0.09, satisfying the LRN condition.

2.2. Materials characterization

Because the polymer we adopted is a frequency-dependent viscoelastic material, frequency-sweeps in dynamic mechanical analysis (DMA, Thermal Analysis System DMA 1, Mettler-Toledo, Switzerland) were conducted. The Kelvin–Voigt model is employed to describe the response of the polymer under a periodic loading with an excitation frequency f. Thus, the relation between the stress σ and strain ε is expressed as [56]:

$$\sigma = E\varepsilon + \gamma \frac{E}{2\pi f}\frac{\partial \varepsilon}{\partial t}, \tag{1}$$

where E and γ are the storage modulus and the loss factor [57]. In DMA, a sample, as shown in figure 2(c), was periodically loaded in the cantilever mode. The force and displacement amplitudes and their phase shift are then analyzed to determine E and γ [58].

The upper limit of the frequency sweep using the DMA is 100 Hz, but the actuation frequency for AFMS is much higher. Hence, the principle of time-temperature superposition (TTS) is employed, which states that a physical property G (representing E and γ) measured under temperature T and frequency f is equivalent to that measured under temperature T_0 and frequency $a_T f$, expressed as [59]:

$$G(f, T) = G(\alpha_T f, T_0), \tag{2}$$

where a_T is the shift factor. WLF equation is employed to determine a_T [60]:

$$\lg \alpha_T = -\frac{C_1 (T - T_0)}{C_2 + (T - T_0)}, \tag{3}$$

where C_1 and C_2 are positive constants dependent on the material and the reference temperature T_0. Using TTS, E and γ measured at different temperatures and frequencies can collapse onto a master curve. In this word, DMA tests were performed for cured Phrozen resins. The reference temperature in the WLF equation (equation (3)) was preset to be room temperature (i.e. $T_0 = 25$ °C). The constants

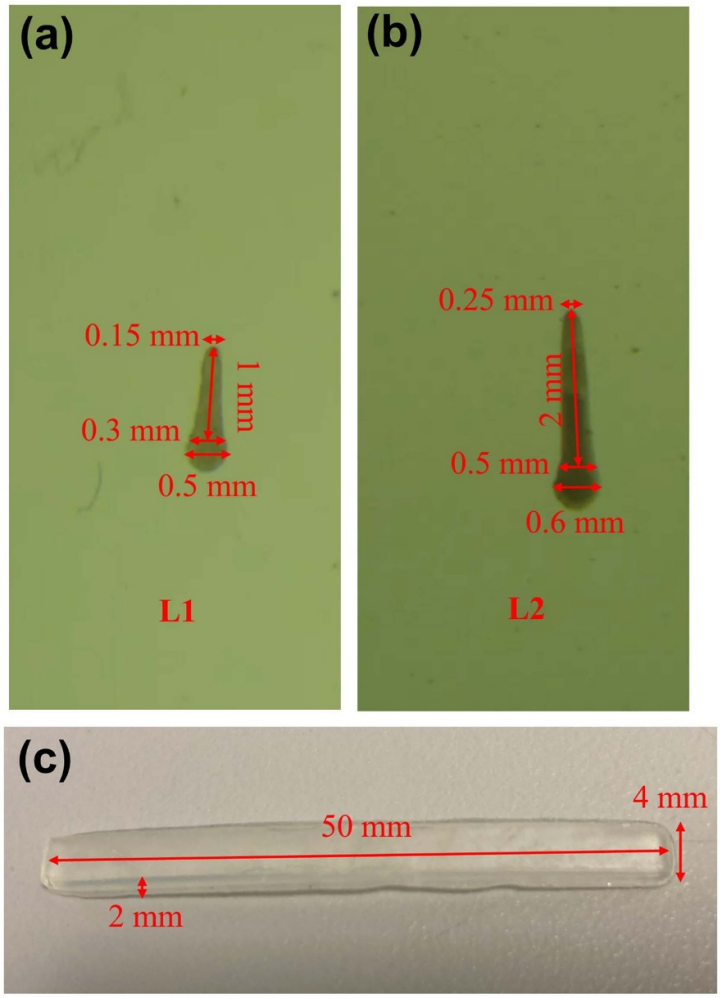

Figure 2. Dimensions of AFMSs and the material sample: (a) the dimensions of AFMS L1, which is around 1 mm long and 0.3 mm thick; (b) the dimensions of AFMS L2, which is around 2 mm long and 0.5 mm thick; (c) the dimensions of the sample for material characterization.

C_1 and C_2 in equation (3) were determined to let all data points collapse to a master curve with minimized deviations.

2.3. Experimental setup

Figure 3 shows an experimental platform of the acoustically actuated AFMS. A polydimethylsiloxane (PDMS) plate with a through slot was fabricated using the standard soft lithography and bonded onto a glass slide to form a swimming channel. A piezoelectric transducer (PZT5 60 × 3 × 0.6 mm^3, Shaoxing Shenlei Ultrasonic Equipment, China) with a resonant frequency of 28 kHz was then attached adjacent to the PDMS channel, where acoustic waves will generate and propagate from the piezoelectric transducer to the fluid inside the channel. Because the sound impedance of the PDMS matches that of the aqueous solution inside the channel, a sound field of traveling waves will prevail if the wall of the PDMS chamber is sufficiently thick [61]. The total thickness of the wall of the chamber is designed to be 10 mm (50 × 20 mm for the outer contour and 35 × 10 mm for the channel), which is much thicker than the channel height of 2 mm and can eliminate the possible reflection of waves from PDMS boundaries.

A waveform generator (DG2052, RIGOL, China) was connected to an amplifier (ATA-2032, AIGTEK, China) to introduce a harmonic waveform to the acoustic transducer and the peak-to-peak voltage (Vpp) is determined by the combination of the generator and amplifier. A stereomicroscope (SZM-6, Weiscope, China) with a high-speed camera (E3ISPM09000KPB 60 fps, Sony, Japan) was used to observe and record the motion of an AFMS. The amplitudes of actuation and swimming velocities of AFMSs can be achieved in terms of different actuation frequencies and voltages.

2.4. Theoretical methods

The details of the CRFT can be found in our previous paper [54]. Here briefly introduced is the concept to address the 2D problem of an AFMS (i.e. with rectangular cross-sections). For a LRN swimming problem, the correction of SBT for the case of non-circular cross-section has been developed in [62] by introducing a dimensionless coefficient tensor **K**. For a

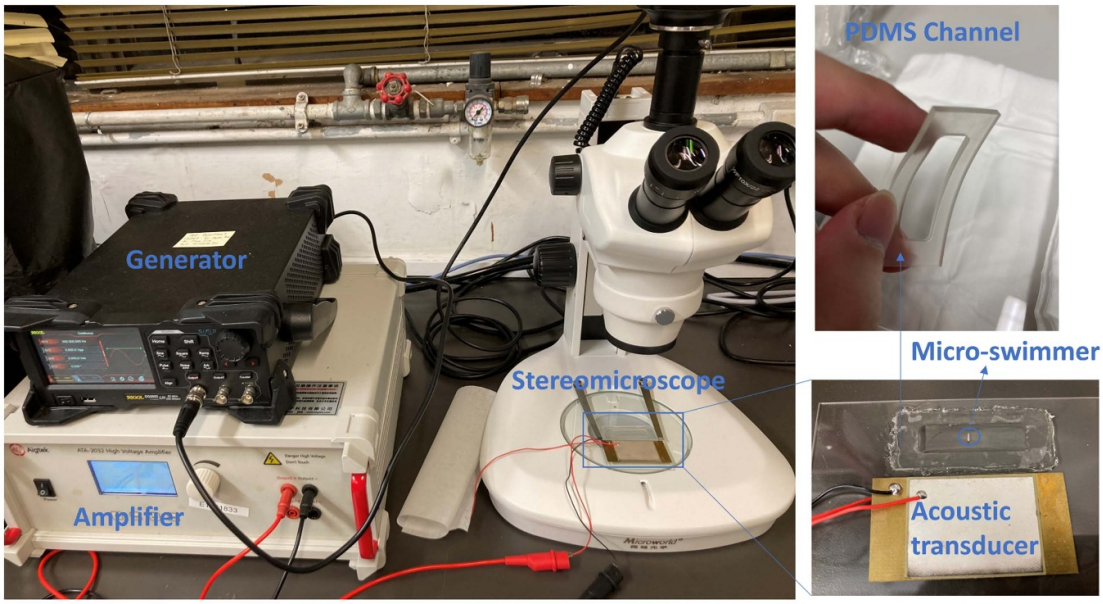

Figure 3. Experimental platform and devices. The inset in the upper right corner shows the flexibility of the PDMS channel; the inset in the lower right corner illustrates how to actuate the micro-swimmer by an acoustic transducer.

slender body with a unit length, let κ denote the half-width of the body, and $\mathbf{u}$ and μ the velocity field and the dynamic viscosity of its surrounding fluid, respectively. For a circular flagellum cross-section, the relative fluid velocity field can be expressed as: $\mathbf{U} = \mathbf{C} \cdot \mathbf{S}$, where $\mathbf{U} = \mathbf{u} - \mathbf{V}$ represents the relative velocity of the fluid with respect to the flagellum part, $\mathbf{C}$ is the resistive tensor, and the Stokeslets $\mathbf{S}$ is based on the expression for a slender body with a circular cross-section [63]. For non-circular ones, it is assumed that the relative fluid velocity for the non-circular case can be expressed as: $\mathbf{U} = (\mathbf{C} + \mathbf{K}) \cdot \mathbf{S}$, where $\mathbf{K} = [K_{ij}]$ $(i, j = 1, 2$ for 2D problems) is the only correction tensor to be determined based on the comparison between FSI simulation and the CRFT model. Denoted by $U_{\parallel}$ and $U_{\perp}$ the components of $\mathbf{U}$ tangential and normal to the local centerline of a flagellum, respectively, the corresponding fluid forces in the RFT are formulated as:

$$F_{f_{\parallel}} = c_{\parallel} U_{\parallel}, F_{f_{\perp}} = c_{\perp} U_{\perp}. \tag{4}$$

After substituting the corrected $\mathbf{U}$ into the expression of $\mathbf{S}$ and adopting an iterative procedure, the two coefficients of resistive forces in the CRFT can be derived as [54]:

$$c_{\parallel} = 2\pi\mu \left[\frac{1}{\ln(1/\kappa)} + \frac{\frac{3}{2} - \ln 2 - \frac{K}{4}}{\ln^2(1/\kappa)} + \frac{\left(\frac{3}{2} - \ln 2 - \frac{K}{4}\right)^2 + 1 - \frac{\pi^2}{12}}{\ln^3(1/\kappa)} \right], \tag{5}$$

$$c_{\perp} = 4\pi\mu \left[\frac{1}{\ln(1/\kappa)} + \frac{\frac{1}{2} - \ln 2 + \frac{K}{2}}{\ln^2(1/\kappa)} + \frac{\left(\frac{1}{2} - \ln 2 + \frac{K}{2}\right)^2 + 1 - \frac{\pi^2}{12}}{\ln^3(1/\kappa)} \right], \tag{6}$$

where the only correction factor $K = K_{11} = -K_{22}$ is in the expression and the second equality is due to the requirement for zero divergence of the tensor $\mathbf{K}$.

The next step is to derive the 2D governing equations of an AFMS. Inspired by Purcell's three-link swimmer [23], a flexible flagellum has been modeled by using multiple rigid bars linked by flexible joints (aka. the bar-joint models) [64], which intrinsically fulfills the inextensible constraints of a flexible tail [65, 66]. We here assume that the flagellum can be simplified into rigid bars with a constant length of $2l$. They are indexed (denoted by i) from 1 to n and connected with linear torsion springs [64]. The ith spring joint connects the bars i and $(i + 1)$ and the first $(i = 1)$ bar is assumed to be rigidly connected to the head. The motion of the ith bar and the head $(i = 0)$ can be represented by the vector of time-dependent variables $\mathbf{X}_i(t) = (x_i, y_i, \theta_i)^{\mathrm{T}}$, where x_i and y_i are coordinates of the midpoint of the ith bar (or the center of the head), and θ_i the angle of rotation with respect to the x-axis (anticlockwise rotation is taken as positive). Correspondingly, the velocity vector of the head $(i = 0)$ and bars $(i > 0)$ can be represented by $\dot{\mathbf{X}}_i = \left(\dot{x}_i, \dot{y}_i, \dot{\theta}_i\right)^{\mathrm{T}}$, where the overhead dot denotes time derivative. Based on the aforementioned Kelvin–Voigt viscoelastic model [56], the moment induced by

the torsion spring at the ith joint M_i is expressed in a forward difference formula as:

$$M_i = E\frac{J_i + J_{i+1}}{2}\frac{\theta_{i+1} - \theta_i}{2l} + \gamma\frac{E}{2\pi f}\frac{J_i + J_{i+1}}{2}\frac{\dot{\theta}_{i+1} - \dot{\theta}_i}{2l}, \tag{7}$$

where J_i denotes the second moment of area of the ith bar, where an average value of J between two neighboring bars is adopted to indicate the second moment of area at the ith joint in case the flagellum is non-uniform. Combining equilibrium equations of forces and moments and constraints, we obtained the equations of motion of the bar-joint model, given by:

$$\begin{bmatrix} \mathbf{A}_0 & \mathbf{A} \\ \mathbf{0} & \mathbf{T}_V \\ -\mathbf{I} & \mathbf{B} \\ \mathbf{D}_0 & \mathbf{D} \end{bmatrix} \begin{bmatrix} \dot{\mathbf{X}}_0 \\ \dot{\mathbf{X}} \end{bmatrix} = \begin{bmatrix} -\mathbf{F}_0 \\ \mathbf{0} \\ \mathbf{0} \\ \mathbf{F}_E \end{bmatrix}, \tag{8}$$

where detailed expressions of all the quantities were reported in our previous work [54].

In equation (8), matrices $\mathbf{A}_0$ and $\mathbf{A}$ represent the effect of fluid resistance on the head and flagellum, respectively. $\mathbf{I}$ is a 3×3 identity matrix, $\mathbf{T}_V$ represents the matrix of kinematic constraints of neighboring bars, and $\mathbf{B}$ is the matrix of the kinematic constraints between the first bar and the head. $\mathbf{D}$ and $\mathbf{D}_0$ are the matrix of moment balance related to the bars and head, respectively. Significantly, the two coefficients of resistive forces $c_{\parallel}$ and $c_{\perp}$ always occur in matrices $\mathbf{A}$ and $\mathbf{D}$, which embodies the effect of K. For the non-homogeneous terms, $\mathbf{F}_0$ is the vector of the external actuation, and $\mathbf{F}_E$ is a list of torques. According to the study of Liu and Ruan [47], the effect of periodic acoustic excitation for an AFMS can be assumed to be a periodic force F_{ext} acting on the head with a frequency f. The head oscillation induced by F_{ext} whips the flagellum, giving rise to the advancement of the AFMS at an average speed of V_{ave}. The term F_{ext} appears in vectors $\mathbf{F}_0$ and $\mathbf{F}_E$, embodying the effect of external actuation. We solved equation (8) by using the built-in ODE solver *ode15s* in MATLAB [67].

The FSI simulations were conducted using a built-in fully coupled 2D FSI solver in COMSOL Multiphysics [68], which was to determine the correction factor K based on the geometry of a printed AFMS. In the numerical simulations, the incompressible creeping flow module without the inertial term (Stokes flow) was employed for the fluid domain, while the solid mechanics module with plane strain approximation for the solid domain [69]. The automatic remeshing technique [70, 71] was employed to tackle the problems induced by large rigid-body motions, where the fluid domain was set as the moving mesh region based on the Winslow smoothing method [72], in which the mesh distortion parameter was set to unity. Other boundary conditions were set as follows: the periodic boundary condition was set on the outer wall of the fluid; on the boundary between the AFMS and the fluid, the wall is set 'no slip'; for the AFMS, the head is set as rigid, and the flagellum is set as viscoelastic; a vertical harmonic force was acted on the head, and the amplitude of the force can be tuned to make sure that the displacement amplitude is identical to that in the experiment. The domain size is physics-controlled, and there is no mesh displacement on the wall of the outer boundary. There is no force-free swimming condition. The details of the FSI simulation can be seen in our precious paper [54], where a mesh convergence study was conducted.

3. Results and discussion

3.1. Results of materials characterization

For the Phrozen resin, the temperature range was from −10 °C to 35 °C with an interval of 5 °C (i.e. 10 sets of data). For each temperature, the loading frequency was from 0.1 Hz to 100 Hz. We determined $C_1 = 40$ and $C_2 = 290$, and the resulting master curves of storage modulus and loss factor in terms of the equivalent frequency (log base) are illustrated in figures 4(a) and (b), respectively. For each temperature, the loading frequency was also from 0.1 Hz to 100 Hz. It is noted that the results of γ do not fit well onto a master curve, and this implies that the TTS assumption does not work well.

3.2. Comparisons between theoretical and experimental results

Directional motions of the AFMSs of the two lengths (i.e. L1 and L2) actuated by sound waves have been observed. The acoustic frequencies were set at 100 and 500 Hz and the Vpps are from 50 to 250 V with an interval of 50 V. Figure 5(a) demonstrates the way to estimate the amplitude of the head oscillation, wherein we take L1 at 100 Hz as an example. Note that the camera on the microscope ran at 60 fps and the AFMS oscillated at 100 Hz. It means that in each frame the camera captured an overlapped image of the AFMS at different positions within one period of oscillation. Hence, the half width of the blurred head of the AFMS image minus the half width of the head renders the amplitude of head oscillation, as shown in figure 5(a). The resonant frequency of the piezoelectric transducer is 28 000 Hz, and the largest frequency we used herein is just 500 Hz. Therefore, the resonance of the transducer does not influence the intensity of the acoustic field. Hence, as shown in figure 5(b), the measured oscillation amplitude of the AFMS is proportional to the input voltage. The difference in the amplitude between L1 and L2 at the same frequency and voltage is indistinguishable.

The terminal velocity averaged within 1 s V_{ave} can be achieved by measuring the distance of swimming captured by the camera. Figure 6(a) exhibits the movement of L1 actuated at 100 Hz and 200 Vpp. The

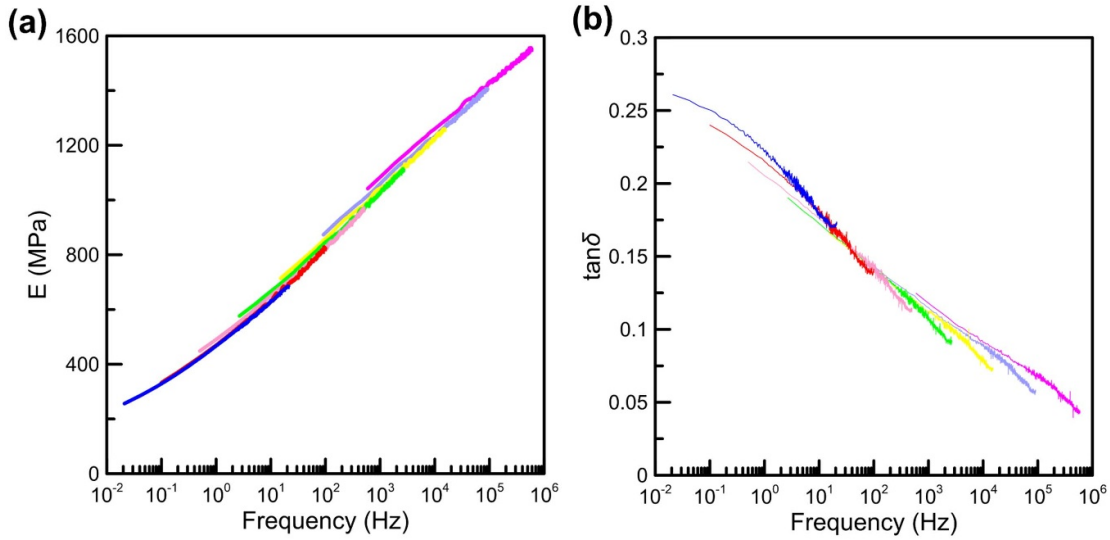

Figure 4. Results of material characterization by TTS test: (a) and (b) are Young's modulus and loss factor in terms of the actuation frequency for the commercial photopolymer, respectively. Different colors indicate different ranges of test temperature, where the actuation frequency ranges are the same for all the tests, which are from 0.1 Hz to 100 Hz.

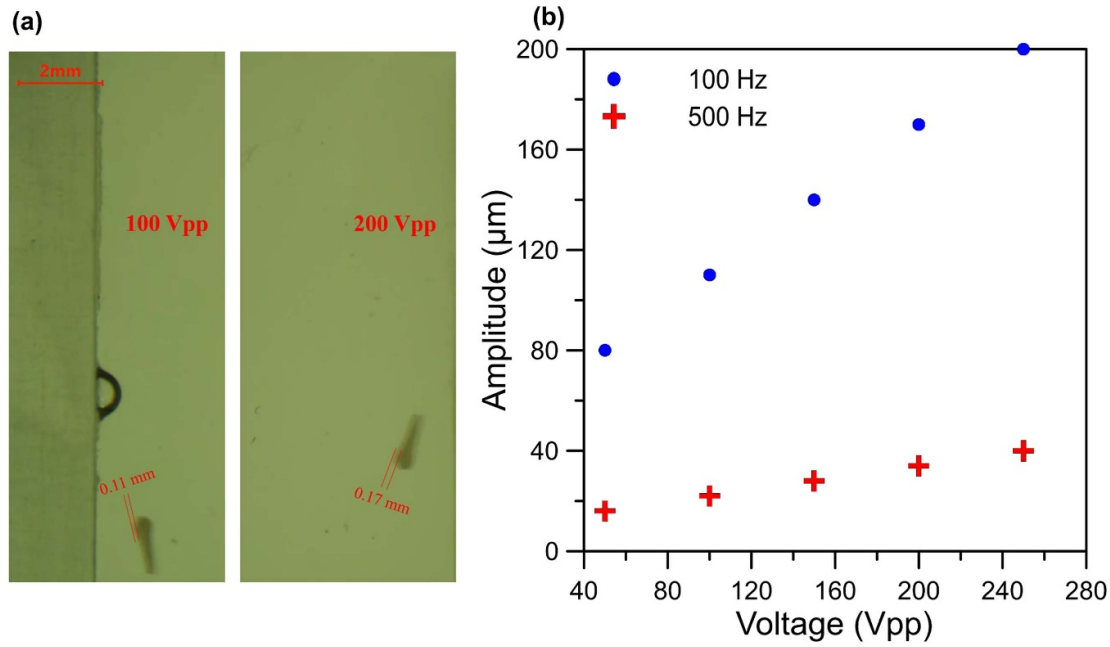

Figure 5. Estimate of actuation amplitudes of AFMSs: (a) an example of extracting the amplitude of an AFMS (dimension L1), where the actuation frequency is 100 Hz, and the measured amplitudes are 0.11 mm for 100 Vpp and 0.17 mm for 200 Vpp, respectively; (b) amplitudes of AFMSs under 5 actuation voltages.

corresponding videos for the experiment and simulation can be seen in the supplementary material. The FSI simulation and the CRFT model can be implemented based on the same actuation conditions and the material parameters characterized above. The corresponding instants of motion in the same time series of the FSI simulation and the CRFT model are shown in figures 6(b) and (c), respectively, where colors on the AFMS in figure 6(b) indicate total displacements, and dotted lines in figure 6(c) indicate the centerline of the flagellum. Note that the red and blue colors in figure 6(b) represent the largest and smallest displacements, respectively. The head is in greenish blue in the second picture of figure 6(b) because the flagellum happens to swing towards the head at that moment; in other cases, the head is in red, which means the flagellum swings away from the head. The comparison among the CRFT model, simulation and experiment results suggests that the FSI simulation and the CRFT model are reliable. The average velocities of the AFMS are determined based on the displacement in 1 s. If reduced the timespan to 1/6 s, i.e. every 10 frames

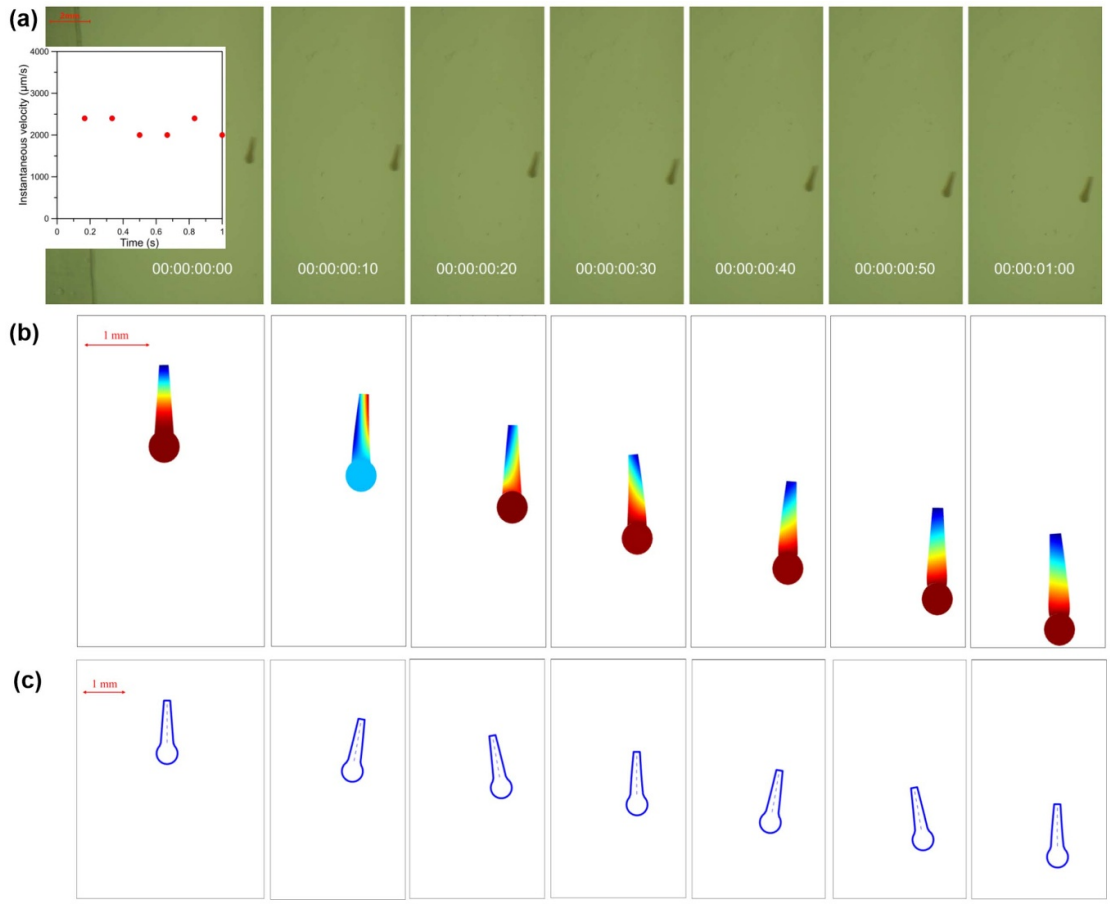

Figure 6. An example of how to estimate the terminal velocity of an AFMS, where the dimension is L1, actuated under 100 Hz and 200 Vpp: (a) screenshots captured by a 60 fps camera within 1 s, the left-hand-side inset is the corresponding velocity variation for every 10 frames (i.e. 1/6 s); (b) results of corresponding FSI simulation within 1 s, where colors on the swimmer indicate displacements; (c) results of the corresponding CRFT model within 1 s, where dotted lines indicate the centerline of the flagellum.

considering the frame rate of 60 per second, the velocities in 1 s vary in a narrow range, as exemplified in the left-hand-side inset of figure 6(a). It is noted that the velocity varies in a narrow range, which is from 2000 to 2400 μm s^{-1}.

Figure 7 illustrates the results of terminal velocities obtained from experiments, FSI simulations and the CRFT model, respectively. Figures 7(a) and (b) are for L1, (c) and (d) for L2. Error bars on the experimental velocities represent the velocity variation within 1 s. Among these results, the largest Re is 0.09 for L2 at 250 Vpp and 100 Hz, which indicates that the swimming problem of the AFMS herein is in the LRN regime, and the theoretical methods based on the RFT should be effective. As shown in figure 7, as expected, the results of the CRFT model conform well to the simulation results. For the experimental ones, it is noted that all the deviations between the experimental results and the simulations are less than 30% for Vpp larger than 160 V and 50% for Vpp less than 160 V. The larger deviation for smaller Vpp might be due to the tendency to enlarge the amplitude of head oscillation in experiments. Because the resolution of the image for recording the head amplitude based on a normal video camera is low, when the amplitude is not large, it is difficult to distinguish the overlapped image of the AFMS. For the same reason, a larger actuation frequency may also cause a larger deviation. In addition, deviations for L1 are overall less than those for L2. The smaller deviation for L1 might be arising from the fact that a smaller swimmer can achieve lower Re and higher effectiveness of the RFT. One may note that both the length of the AFMS and the actuation frequency for figure 7(d) are large, it could be understood that the deviation in figure 7(d) is the largest within the four cases.

Several causes of deviations must be stressed. First, the extrapolated viscoelastic parameters of the AFMS material based on the TTS introduced errors; second, the head oscillation amplitude determined based on a normal video camera has limited accuracy; third, the experimental AFMS has a finite depth, but the numerical model is two-dimensional (i.e. infinite depth). These issues all contributed to the 30%–50%

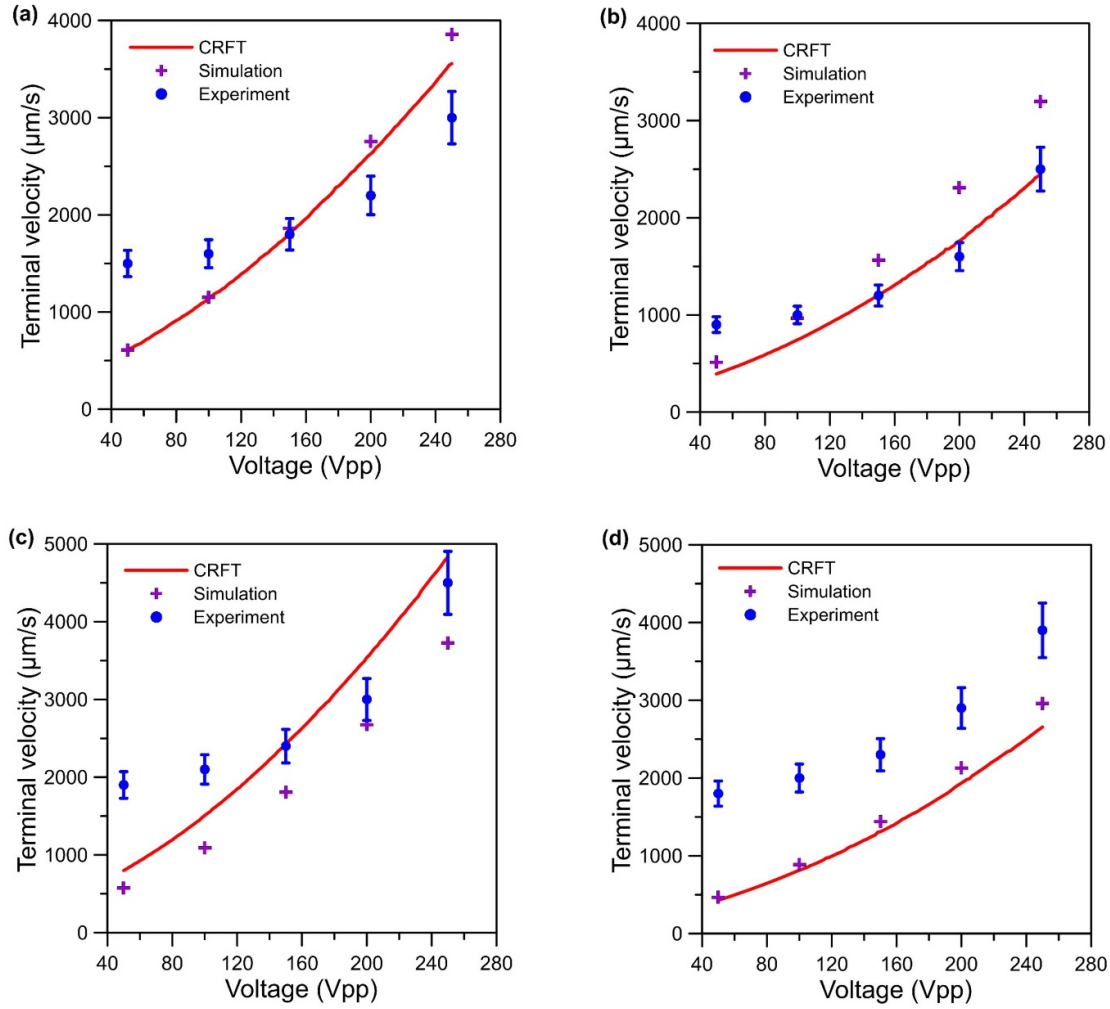

Figure 7. Results of terminal velocities versus Vpps (peak-to-peak voltages in the unit of V) obtained from experiments, FSI simulations and the CRFT model, respectively, with parameters of: (a) dimension L1 under 100 Hz, $K = 94$ for the CRFT model; (b) dimension L1 under 500 Hz, $K = 86$ for the CRFT model; (c) dimension L2 under 100 Hz, $K = 160$ for the CRFT model; (d) dimension L2 under 500 Hz, $K = 177$ for the CRFT model.

errors in the prediction of the motilities of the AFMSs. It is noted that most of investigations of AFMSs lack of theoretical analyses [19, 52]. Some used the computational results of acoustic streaming to determine motility but failed to achieve meaningful comparison. For example, there is nearly a 300% deviation in the optimal actuation frequency given in [18]; or the errors of streaming speeds (not the terminal velocities of AFMSs) are around 50% [33]. Thus, we think that such a level of deviation is reasonable and acceptable. One may note that for a small actuation voltage, the experimental velocity is larger than that of simulation. While, for a large actuation voltage, the experimental one is smaller than that of simulation. This phenomenon can be explained as follows. For an ideal head-actuated flagellated micro-swimmer, theoretical and computational models indicate that the swimming velocity is proportional to the square of head oscillation amplitude [47, 73], and the amplitude is proportional to the applied voltage (as shown in figure 5(b)), thus the velocity should be proportional to the square of the applied voltage. However, in the actual case, the proportionality between the velocity and the square of the amplitude may not hold. The deviation could be caused by the complex flows adjacent to the junction of head and flagellum and to the tip of the flagellum; and as we have mentioned before, our 2D simulation (infinite depth) cannot address the case of the practical swimmer with a finite thickness. These complex flows generally lead to more drags and make the relation between the velocity and the amplitude follows a power law with an exponent less than 2. In our experiments, it is noted that the relation between the velocity and applied voltage follows a power law with an exponent less than 2. In this case, with the increase in actuation voltage, the simulated velocity will be larger than that of experiment sooner or later. For figures 7(c) and (d), although the results of simulation are all less than those of experiment, the trend of the curves indicates that the

simulation results will eventually larger than experimental ones when the actuation voltage is very large.

4. Conclusions

We established a testing platform to experimentally verify the theoretical calculations of the AFMSs actuated by acoustic waves based on the CRFT and the bar-joint model proposed in our previous work. We demonstrated the printed AFMSs using a DLP printer and characterized the viscoelastic properties of the UV-cured resins. After that, we described the setup of the experimental platform for observing the motion of an acoustically actuated AFMS. Swimming velocities obtained from experiments, FSI simulations and CRFT models were presented and compared. The deviations are within 50%, corroborating that our theoretical treatment of the acoustic actuation for a head-flagellum structure is sensible.

Further investigations could focus on the theoretical models and experimental verifications of the influences of shapes of AFMSs and the effect of complex fluids. For example, the influence of tapering or the width-to-length ratio of the flagellum could be experimentally verified by fabricating more AFMSs with different combinations of flagellum shapes. The modeling and experimental verifying of the AFMS with a helical flagellum or multi-flagellum is also a topic of general interest. While our method can be used in different environments, adjustments are often necessary to account for the medium-specific attenuation effects. For example, the bodily fluids are often non-Newtonian, which introduces nonlinearities to the system. Ouyang *et al* [74] reported the locomotion of a cargo-carrying micro-swimmer through shear-dependent non-Newtonian fluids by simulations. In the future, we may try to establish an experimental platform with non-Newtonian fluids to verify their theoretical results if possible.

Data availability statement

All data that support the findings of this study are included within the article (and any supplementary files).

Acknowledgments

This work was financially supported by NSFC/RGC Joint Research Scheme (Project Number: N_PolyU519/19). The authors are grateful for the financial supports.

ORCID iDs

Jinan Liu https://orcid.org/0000-0002-9511-4881
Haihui Ruan https://orcid.org/0000-0002-9233-8820

References

[1] Yang G-Z, Fischer P and Nelson B 2017 New materials for next-generation robots *Sci. Robot.* **2** eaap9294
[2] Patra D, Sengupta S, Duan W, Zhang H, Pavlick R and Sen A 2013 Intelligent, self-powered, drug delivery systems *Nanoscale* **5** 1273–83
[3] Ma X, Hahn K and Sanchez S 2015 Catalytic mesoporous Janus nanomotors for active cargo delivery *J. Am. Chem. Soc.* **137** 4976–9
[4] Medina-Sánchez M, Schwarz L, Meyer A K, Hebenstreit F and Schmidt O G 2016 Cellular cargo delivery: toward assisted fertilization by sperm-carrying micromotors *Nano Lett.* **16** 555–61
[5] Walker D, Käsdorf B T, Jeong H-H, Lieleg O and Fischer P 2015 Enzymatically active biomimetic micropropellers for the penetration of mucin gels *Sci. Adv.* **1** e1500501
[6] Miyashita S, Guitron S, Yoshida K, Li S, Damian D D and Rus D 2016 Ingestible, controllable, and degradable origami robot for patching stomach wounds *2016 IEEE Int. Conf. on Robotics and Automation (ICRA)* (IEEE)
[7] Soler L, Magdanz V, Fomin V M, Sanchez S and Schmidt O G 2013 Self-propelled micromotors for cleaning polluted water *ACS Nano* **7** 9611–20
[8] Soler L and Sánchez S 2014 Catalytic nanomotors for environmental monitoring and water remediation *Nanoscale* **6** 7175–82
[9] Vilela D, Parmar J, Zeng Y, Zhao Y and Sánchez S 2016 Graphene-based microbots for toxic heavy metal removal and recovery from water *Nano Lett.* **16** 2860–6
[10] Feng J and Cho S K 2014 Mini and micro propulsion for medical swimmers *Micromachines* **5** 97–113
[11] Liu J, Fu Y, Liu X and Ruan H 2021 Theoretical perspectives on natural and artificial micro-swimmers *Acta Mech. Solida Sin.* **34** 783–809
[12] Dijkink R, Van Der Dennen J, Ohl C and Prosperetti A 2006 The 'acoustic scallop': a bubble-powered actuator *J. Micromech. Microeng.* **16** 1653
[13] Bertin N, Spelman T A, Stephan O, Gredy L, Bouriau M, Lauga E and Marmottant P 2015 Propulsion of bubble-based acoustic microswimmers *Phys. Rev. Appl.* **4** 064012
[14] Wang W, Castro L A, Hoyos M and Mallouk T E 2012 Autonomous motion of metallic microrods propelled by ultrasound *ACS Nano* **6** 6122–32
[15] Li T, Li J, Zhang H, Chang X, Song W, Hu Y, Shao G, Sandraz E, Zhang G and Li L 2016 Nanorobots: magnetically propelled fish-like nanoswimmers (small 44/2016) *Small* **12** 6045
[16] Zhang L, Abbott J J, Dong L, Kratochvil B E, Bell D and Nelson B J 2009 Artificial bacterial flagella: fabrication and magnetic control *Appl. Phys. Lett.* **94** 064107
[17] Schuerle S, Pané S, Pellicer E, Sort J, Baró M D and Nelson B J 2012 Helical and tubular lipid microstructures that are electroless-coated with CoNiReP for wireless magnetic manipulation *Small* **8** 1498–502
[18] Ahmed D, Baasch T, Jang B, Pane S, Dual J and Nelson B J 2016 Artificial swimmers propelled by acoustically activated flagella *Nano Lett.* **16** 4968–74
[19] Kaynak M, Ozcelik A, Nourhani A, Lammert P E, Crespi V H and Huang T J 2017 Acoustic actuation of bioinspired microswimmers *Lab Chip* **17** 395–400
[20] Lauga E and Powers T R 2009 The hydrodynamics of swimming microorganisms *Rep. Prog. Phys.* **72** 096601
[21] Sitti M, Ceylan H, Hu W, Giltinan J, Turan M, Yim S and Diller E 2015 Biomedical applications of untethered mobile milli/microrobots *Proc. IEEE* **103** 205–24
[22] Kadry H, Wadnap S, Xu C and Ahsan F 2019 Digital light processing (DLP) 3D-printing technology and photoreactive polymers in fabrication of modified-release tablets *Eur. J. Pharm. Sci.* **135** 60–67
[23] Purcell E M 1977 Life at low Reynolds number *Am. J. Phys.* **45** 3–11

[24] Chen X Z, Jang B, Ahmed D, Hu C, De Marco C, Hoop M, Mushtaq F, Nelson B J and Pané S 2018 Small-scale machines driven by external power sources *Adv. Mater.* **30** 1705061
[25] Hussein H, Damdam A, Ren L, Obeid Charrouf Y, Challita J, Zwain M and Fariborzi H 2023 Actuation of mobile microbots: a review *Adv. Intell. Syst.* **5** 2300168
[26] Liang X, Chen Z, Deng Y, Liu D, Liu X, Huang Q and Arai T 2023 Field-controlled microrobots fabricated by photopolymerization *Cyborg Bionic Syst.* **4** 0009
[27] Ni M, Leung M K, Leung D Y and Sumathy K 2007 A review and recent developments in photocatalytic water-splitting using TiO_2 for hydrogen production *Renew. Sustain. Energy Rev.* **11** 401–25
[28] Saito K, Iwata K, Ishihara Y, Sugita K, Takato M and Uchikoba F 2016 Miniaturized rotary actuators using shape memory alloy for insect-type MEMS microrobot *Micromachines* **7** 58
[29] Zhou H, Mayorga-Martinez C C, Pané S, Zhang L and Pumera M 2021 Magnetically driven micro and nanorobots *Chem. Rev.* **121** 4999–5041
[30] Rao K J, Li F, Meng L, Zheng H, Cai F and Wang W 2015 A force to be reckoned with: a review of synthetic microswimmers powered by ultrasound *Small* **11** 2836–46
[31] Mohanty S, Khalil I S and Misra S 2020 Contactless acoustic micro/nano manipulation: a paradigm for next generation applications in life sciences *Proc. R. Soc.* A **476** 20200621
[32] Ovchinnikov M, Zhou J and Yalamanchili S 2014 Acoustic streaming of a sharp edge *J. Acoust. Soc. Am.* **136** 22–29
[33] Kaynak M, Ozcelik A, Nama N, Nourhani A, Lammert P E, Crespi V H and Huang T J 2016 Acoustofluidic actuation of in situ fabricated microrotors *Lab Chip* **16** 3532–7
[34] Nama N, Huang P-H, Huang T J and Costanzo F 2014 Investigation of acoustic streaming patterns around oscillating sharp edges *Lab Chip* **14** 2824–36
[35] Rorai C, Zaitsev M and Karabasov S 2019 On the limitations of some popular numerical models of flagellated microswimmers: importance of long-range forces and flagellum waveform *R. Soc. Open Sci.* **6** 180745
[36] Hancock G J 1953 The self-propulsion of microscopic organisms through liquids *Proc. R. Soc.* A **217** 96–121
[37] Newman J N 1964 A slender-body theory for ship oscillations in waves *J. Fluid Mech.* **18** 602–18
[38] Cox R 1970 The motion of long slender bodies in a viscous fluid Part 1. General theory *J. Fluid Mech.* **44** 791–810
[39] Keller J B and Rubinow S I 1976 Slender-body theory for slow viscous flow *J. Fluid Mech.* **75** 705–14
[40] Koens L and Lauga E 2018 The boundary integral formulation of Stokes flows includes slender-body theory *J. Fluid Mech.* **850** R1
[41] Rodenborn B, Chen C-H, Swinney H L, Liu B and Zhang H 2013 Propulsion of microorganisms by a helical flagellum *Proc. Natl Acad. Sci.* **110** E338–47
[42] Zhang T and Goldman D I 2014 The effectiveness of resistive force theory in granular locomotion *Phys. Fluids* **26** 101308
[43] Gray J and Hancock G 1955 The propulsion of sea-urchin spermatozoa *J. Exp. Biol.* **32** 802–14
[44] Lighthill J 1976 Flagellar hydrodynamics *SIAM Rev.* **18** 161–230
[45] Gauger E and Stark H 2006 Numerical study of a microscopic artificial swimmer *Phys. Rev.* E **74** 021907
[46] Ahmed S, Wang W, Bai L, Gentekos D T, Hoyos M and Mallouk T E 2016 Density and shape effects in the acoustic propulsion of bimetallic nanorod motors *ACS Nano* **10** 4763–9
[47] Liu J and Ruan H 2020 Modeling of an acoustically actuated artificial micro-swimmer *Bioinsp. Biomim.* **15** 036002
[48] Deng Y, Paskert A, Zhang Z, Wittkowski R and Ahmed D 2023 An acoustically controlled helical microrobot *Sci. Adv.* **9** eadh5260
[49] Chen Z, Li J, Liu C, Liu Y, Zhu J and Lao C 2019 Preparation of high solid loading and low viscosity ceramic slurries for photopolymerization-based 3D printing *Ceram. Int.* **45** 11549–57
[50] Barone S, Neri P, Paoli A and Razionale A 2020 3D acquisition and stereo-camera calibration by active devices: a unique structured light encoding framework *Opt. Lasers Eng.* **127** 105989
[51] Zhou Y, Wang H, Ma Z, Yang J K and Ai Y 2020 Acoustic vibration-induced actuation of multiple microrotors in microfluidics *Adv. Mater. Technol.* **5** 2000323
[52] Xiao Y, Zhang J, Zhao X, Fang B, Ma L and Hao N 2023 An artificial acoustics-actuated microrobot bioinspired by Chlamydomonas *Sens. Actuators* A **361** 114592
[53] Xiao Y, Zhang J, Fang B, Zhao X and Hao N 2022 Acoustics-actuated microrobots *Micromachines* **13** 481
[54] Liu J, Fu Y, Liu X and Ruan H 2023 A bar-joint model based on the corrected resistive force theory for artificial flagellated micro-swimmers propelled by acoustic waves *Bioinsp. Biomim.* **18** 035003
[55] Hwang K S, Ju S H, Kwon H J, Kim Y, Lee C, Koh W G, Choi W J and Lee J Y 2022 Feasible digital light processing three-dimensional printing of a biodegradable porous polymer with a high internal phase emulsion structure *ACS Appl. Polym. Mater.* **4** 1570–5
[56] Odegard G, Gates T and Herring H 2005 Characterization of viscoelastic properties of polymeric materials through nanoindentation *Exp. Mech.* **45** 130–6
[57] Ghayesh M H 2019 Viscoelastic dynamics of axially FG microbeams *Int. J. Eng. Sci.* **135** 75–85
[58] Chartoff R P, Menczel J D and Dillman S H 2009 Dynamic mechanical analysis (DMA) *Thermal Analysis of Polymers: Fundamentals and Applications* pp 387–495
[59] Ferry J D 1980 *Viscoelastic Properties of Polymers* (Wiley)
[60] Williams M L, Landel R F and Ferry J D 1955 The temperature dependence of relaxation mechanisms in amorphous polymers and other glass-forming liquids *J. Am. Chem. Soc.* **77** 3701–7
[61] Leibacher I, Schatzer S and Dual J 2014 Impedance matched channel walls in acoustofluidic systems *Lab Chip* **14** 463–70
[62] Batchelor G K 1970 Slender-body theory for particles of arbitrary cross-section in Stokes flow *J. Fluid Mech.* **44** 419–40
[63] Chwang A T and Wu T Y-T 1975 Hydromechanics of low-Reynolds-number flow. Part 2. Singularity method for Stokes flows *J. Fluid Mech.* **67** 787–815
[64] Alouges F, DeSimone A, Giraldi L and Zoppello M 2015 Can magnetic multilayers propel artificial microswimmers mimicking sperm cells? *Soft Robot.* **2** 117–28
[65] Pak O S, Lauga E, Duprat C and Stone H 2015 Theoretical models of low-Reynolds-number locomotion *Fluid-Structure Interactions in Low-Reynolds-Number Flows* (Royal Society of Chemistry) pp 100–67
[66] Dowell E and McHugh K 2016 Equations of motion for an inextensible beam undergoing large deflections *J. Appl. Mech.* **83** 051007
[67] Kuhn L M, Russell S, Boudreaux M, Gaboury J and Maulding B 2019 Development of a rapid first-order differential equation solver for stiff systems *Proc. Int. Conf. on Scientific Computing (CSC): The Steering Committee of the World Congress in Computer Science, Computer Engineering and Applied Computing*
[68] Curtis F G, Ekici K and Freels J D 2011 Fluid-structure interaction for coolant flow in research-type nuclear reactors *COMSOL Conf.*
[69] Christian J T and Boehmer J W 1970 Plane strain consolidation by finite elements *J. Soil Mech. Found. Div.* **96** 1435–57
[70] Germann P, Menshykau D, Tanaka S and Iber D 2012 Simulating organogenesis in COMSOL (arXiv:1202.0428)
[71] Cordovilla F, García-Beltrán Á, Garzón M, Muñoz D A and Ocaña J L 2018 Numerical-experimental study of the

consolidation phenomenon in the selective laser melting process with a thermo-fluidic coupled model *Materials* **11** 1414

[72] Winslow A M 1966 Numerical solution of the quasilinear Poisson equation in a nonuniform triangle mesh *J. Comput. Phys.* **1** 149–72

[73] Wiggins C H and Goldstein R E 1998 Flexive and propulsive dynamics of elastica at low Reynolds number *Phys. Rev. Lett.* **80** 3879

[74] Ouyang Z, Liu C, Qi T, Lin J and Ku X 2023 Locomotion of a micro-swimmer towing load through shear-dependent non-Newtonian fluids *Phys. Fluids* **35** 013334